



Universiteit  
Leiden  
The Netherlands

## Warm and cold gas in low-mass protostars : Herschel Space Observatory and ground-based surveys

Yildiz, U

### Citation

Yildiz, U. (2013, May 1). *Warm and cold gas in low-mass protostars : Herschel Space Observatory and ground-based surveys*. Retrieved from <https://hdl.handle.net/1887/20855>

Version: Not Applicable (or Unknown)

License: [Leiden University Non-exclusive license](#)

Downloaded from: <https://hdl.handle.net/1887/20855>

**Note:** To cite this publication please use the final published version (if applicable).

Cover Page



Universiteit Leiden



The handle <http://hdl.handle.net/1887/20855> holds various files of this Leiden University dissertation.

**Author:** Yildiz, Umut

**Title:** Warm and cold gas in low-mass protostars : Herschel Space Observatory and ground-based surveys

**Issue Date:** 2013-05-01



*Herschel-HIFI observations of  
high-J CO lines in the NGC 1333  
low-mass star-forming region*

U.A. Yıldız, E.F. van Dishoeck, L.E. Kristensen, R. Visser, J.K. Jørgensen, G.J. Herczeg, T.A. van Kempen, M.R. Hogerheijde, S.D. Doty, A.O. Benz, S. Bruderer, S.F. Wampfler, E. Deul, R. Bachiller, A. Baudry, M. Benedettini, E. Bergin, P. Bjerkeli, G.A. Blake, S. Bontemps, J. Braine, P. Caselli, J. Cernicharo, C. Codella, F. Daniel, A.M. di Giorgio, C. Dominik, P. Encrenaz, M. Fich, A. Fuente, T. Giannini, J.R. Goicoechea, Th. de Graauw, F. Helmich, F. Herpin, T. Jacq, D. Johnstone, B. Larsson, D. Lis, R. Liseau, F.-C. Liu, M. Marseille, C. M<sup>c</sup>Coey, G. Melnick, D. Neufeld, B. Nisini, M. Olberg, B. Parise, J.C. Pearson, R. Plume, C. Risacher, J. Santiago-García, P. Saraceno, R. Shipman, M. Tafalla, A. G. G. M. Tielens, F. van der Tak, F. Wyrowski, P. Dieleman, W. Jellema, V. Ossenkopf, R. Schieder, J. Stutzki  
*Astronomy & Astrophysics*, 2010, Volume 521, L40

## Abstract

In this chapter, we study the *Herschel*-HIFI observations of high- $J$  lines (up to  $J_u=10$ ) of  $^{12}\text{CO}$ ,  $^{13}\text{CO}$  and  $\text{C}^{18}\text{O}$  are presented toward three deeply embedded low-mass protostars, NGC 1333 IRAS 2A, IRAS 4A, and IRAS 4B, obtained as part of the *Water In Star-forming regions with Herschel* (WISH) key program. The spectrally-resolved HIFI data are complemented by ground-based observations of lower- $J$  CO and isotopologue lines. The  $^{12}\text{CO}$  10–9 profiles are dominated by broad (FWHM 25–30 km s $^{-1}$ ) emission. Radiative transfer models are used to constrain the temperature of this shocked gas to 100–200 K. Several CO and  $^{13}\text{CO}$  line profiles also reveal a medium-broad component (FWHM 5–10 km s $^{-1}$ ), seen prominently in  $\text{H}_2\text{O}$  lines. Column densities for both components are presented, providing a reference for determining abundances of other molecules in the same gas. The narrow  $\text{C}^{18}\text{O}$  9–8 lines probe the warmer part of the quiescent envelope. Their intensities require a jump in the CO abundance at an evaporation temperature around 25 K, thus providing new direct evidence for a CO ice evaporation zone around low-mass protostars.

## 2.1 Introduction

The earliest protostellar phase just after cloud collapse – the so-called Class 0 phase – is best studied at mid-infrared and longer wavelengths (André et al. 2000). To understand the physical and chemical evolution of low-mass protostars, in particular the relative importance of radiative heating and shocks in their energy budget, observations are required that can separate these components. The advent of the Heterodyne Instrument for the Far-Infrared (HIFI) on *Herschel* opens up the possibility to obtain spectrally resolved data from higher-frequency lines that are sensitive to gas temperatures up to several hundred Kelvin.

Because of its high abundance and strong lines, CO is the primary molecule to probe the various components of protostellar systems (envelope, outflow, disk). The main advantage of CO compared with other molecules (including water) is that its chemistry is simple, with most carbon locked up in CO in dense clouds. Also, its evaporation temperature is low, around 20 K for pure CO ice (Collings et al. 2003, Öberg et al. 2005), so that its freeze-out zone is much smaller than that of water. Most ground-based observations of CO and its isotopologues have been limited to the lowest rotational lines originating from levels up to 35 K. ISO has detected strong far-infrared CO lines up to  $J_u=29$  from Class 0 sources (Giannini et al. 2001) but the emission is spatially unresolved in the large 80'' beam. ISO also lacked the spectral resolution needed to separate the shocked and quiescent gas or to detect intrinsically-weaker  $^{13}\text{CO}$  and  $\text{C}^{18}\text{O}$  lines on top of the strong continuum.

The NGC 1333 region in Perseus ( $d = 235$  pc; Hirota et al. 2008) contains several deeply embedded Class 0 sources within a  $\sim 1$  pc region driving powerful outflows (e.g., Liseau et al. 1988, Hatchell & Fuller 2008). The protostars IRAS 4A and 4B, separated by  $\sim 31''$ , and IRAS 2A are prominent submillimeter continuum sources (luminosities of 5.8, 3.8 and  $20 L_\odot$ ) with envelope masses of 4.5, 2.9 and  $1.0 M_\odot$ , respectively (Sandell et al. 1991, Jørgensen et al. 2009). All three are among the brightest and best studied low-mass sources in terms of molecular lines, with several complex molecules detected (e.g., Blake et al. 1995, Bottinelli et al. 2007). Here HIFI data of CO and its isotopologues are presented for these three sources and used to quantify the different physical components. In an accompanying letter, Kristensen et al. (2010) present complementary HIFI observations of  $\text{H}_2\text{O}$  and analyze CO/ $\text{H}_2\text{O}$  abundance ratios.

## 2.2 Observations and results

The NGC 1333 data were obtained with HIFI (de Graauw et al. 2010) onboard the *Herschel* Space Observatory (Pilbratt et al. 2010), in the context of the WISH key program (van Dishoeck et al. 2011). Single pointings at the three source positions were carried out between 2010 March 3 and 15 during the *Herschel* HIFI priority science program (PSP). Spectral lines were observed in dual-beam switch (DBS) mode in HIFI bands

**Table 2.1** – Overview of the observations of IRAS 2A, 4A, and 4B.

| Mol.                    | Trans. | $E_u/k_B$<br>(K) | Frequency<br>(GHz) | Tel./Inst. | Beam<br>size (a) | Ref. |
|-------------------------|--------|------------------|--------------------|------------|------------------|------|
| CO                      | 2–1    | 16.6             | 230.538            | JCMT       | 22               | 1    |
|                         | 4–3    | 55.3             | 461.041            | JCMT       | 11               | 2    |
|                         | 6–5    | 116.2            | 691.473            | APEX       | 9                | 3    |
|                         | 10–9   | 304.2            | 1151.985           | HIFI-5a    | 20               | 4    |
| $^{13}\text{CO}$        | 10–9   | 290.8            | 1101.349           | HIFI-4b    | 21               | 4    |
| $\text{C}^{18}\text{O}$ | 1–0    | 5.3              | 109.782            | Onsala     | 34               | 1    |
|                         | 2–1    | 15.8             | 219.560            | JCMT       | 23               | 1    |
|                         | 3–2    | 31.6             | 329.331            | JCMT       | 15               | 1    |
|                         | 5–4    | 79.0             | 548.831            | HIFI-1a    | 42               | 4    |
|                         | 6–5    | 110.6            | 658.553            | APEX       | 10               | 3    |
|                         | 9–8    | 237.0            | 987.560            | HIFI-4a    | 23               | 4    |
|                         | 10–9   | 289.7            | 1097.162           | HIFI-4b    | 21               | 4    |

**Notes.** (1) Jørgensen et al. (2002); (2) JCMT archive; (3) Yıldız et al. (2012); (4) this work

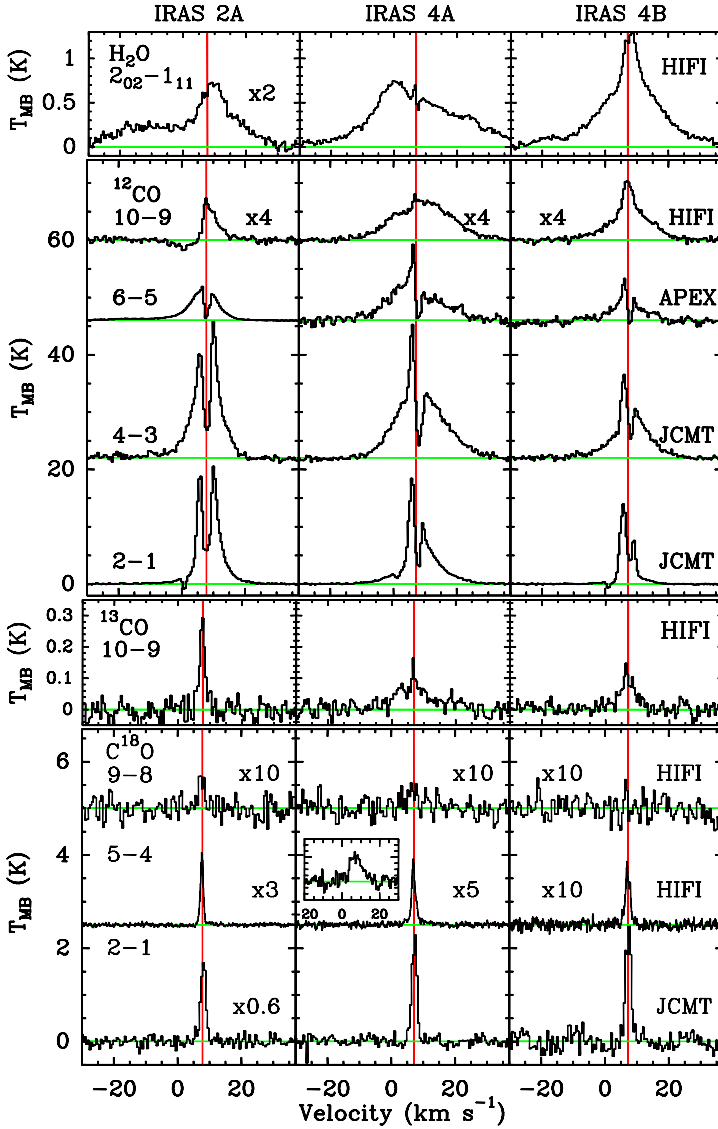
1a, 4a, 4b, and 5a with a chop reference position located 3' from the source positions. The observed positions (J2000) are: IRAS 2A:  $3^{\text{h}}28^{\text{m}}55^{\text{s}}.6$ ,  $+31^{\circ}14'37.''1$ ; IRAS 4A:  $3^{\text{h}}29^{\text{m}}10^{\text{s}}.5$ ,  $+31^{\circ}13'30.''9$ ; and IRAS 4B:  $3^{\text{h}}29^{\text{m}}12^{\text{s}}.0$ ,  $+31^{\circ}13'08.''1$  (Jørgensen et al. 2009).

Table 2.1 summarizes the lines observed with HIFI together with complementary lower- $J$  lines obtained with ground-based telescopes. The *Herschel* data were taken using the wide band spectrometer (WBS) and high resolution spectrometer (HRS) backends. Owing to the higher noise ( $\sqrt{2}$  more) in HRS than WBS, mainly WBS data are presented here. Only the narrow  $\text{C}^{18}\text{O}$  5–4 lines use the HRS data. Integration times (on+off) are 10, 20, 30, 40, and 60 minutes for the  $^{12}\text{CO}$  10–9,  $\text{C}^{18}\text{O}$  9–8, 10–9,  $^{13}\text{CO}$  10–9, and  $\text{C}^{18}\text{O}$  5–4 lines respectively. The HIFI beam sizes correspond to  $\sim 20''$  ( $\sim 4700$  AU) at 1152 GHz and  $\sim 42''$  ( $\sim 10000$  AU) at 549 GHz. Except for the  $^{12}\text{CO}$  10–9 line, all isotopologue lines were observed together with  $\text{H}_2\text{O}$  lines.

The calibration uncertainty for the HIFI data is of the order of 20% and the pointing accuracy is around 2''. The measured line intensities were converted to the main-beam brightness temperatures  $T_{\text{MB}} = T_A^*/\eta_{\text{MB}}$  by using a beam efficiency  $\eta_{\text{MB}} = 0.74$  for all HIFI lines. Data processing started from the standard HIFI pipeline in the *Herschel* interactive processing environment (HIPE<sup>1</sup>) ver. 3.0.1 (Ott 2010), where the  $V_{\text{LSR}}$  precision is of the order of a few  $\text{m s}^{-1}$ . Further reduction and analysis were done using the GILDAS-CLASS<sup>2</sup> software. The spectra from the H- and V-polarizations were averaged in order to obtain a better  $S/N$ . In some cases a discrepancy of 30% was found between the two polarizations, in which case only the H band spectra were used for analysis since their rms is lower.

<sup>1</sup> HIPE is a joint development by the *Herschel* Science Ground Segment Consortium, consisting of ESA, the NASA *Herschel* Science Center, and the HIFI, PACS and SPIRE consortia.

<sup>2</sup> <http://www.iram.fr/IRAMFR/GILDAS/>



**Figure 2.1** – Spectra at the central positions of IRAS 2A, 4A and 4B. *Top to bottom*:  $\text{H}_2\text{O}$   $2_{02}-1_{11}$  line from Kristensen et al. (2010) illustrating the medium and broad components, and spectra of  $^{12}\text{CO}$ ,  $^{13}\text{CO}$ , and  $\text{C}^{18}\text{O}$ . The red lines correspond to the source velocities as obtained from the low- $J$   $\text{C}^{18}\text{O}$  lines. The insert in the  $\text{C}^{18}\text{O}$   $5-4$  line for IRAS 4A illustrates the weak medium component with peak  $T_{\text{MB}} = 22$  mK obtained after subtracting a Gaussian fit to the narrow line.

**Table 2.2** – Observed line intensities.

| Source                  | Mol.                    | Trans.  | $\int T_{\text{MB}} dV$<br>(K km s $^{-1}$ ) | $T_{\text{peak}}$<br>(K) | rms $^a$<br>(K) |      |      |
|-------------------------|-------------------------|---------|--|--------------------------|-----------------|------|------|
| IRAS 2A                 | CO                      | 2–1     | 127.5  | 20.5                     | 0.08            |      |      |
|                         |                         | 4–3     | 177.2  | 23.8                     | 0.44            |      |      |
|                         |                         | 6–5     | 57.0   | 5.9                      | 0.11            |      |      |
|                         |                         | 10–9    | 16.3   | 1.71                     | 0.078           |      |      |
|                         | $^{13}\text{CO}$        | 10–9    | 0.4  | 0.3                      | 0.026           |      |      |
|                         | $\text{C}^{18}\text{O}$ | 1–0     | 5.6  | 4.0                      | 0.27            |      |      |
|                         |                         | 2–1     | 5.83   | 2.3                      | 0.15            |      |      |
|                         |                         | 3–2     | 4.7  | 3.2                      | 0.13            |      |      |
|                         |                         | 5–4     | 0.62   | 0.46                     | 0.004           |      |      |
|                         |                         | 6–5     | 1.8  | 1.1                      | 0.11            |      |      |
|                         |                         | 9–8     | 0.2  | 0.07                     | 0.018           |      |      |
|                         |                         | 10–9    | 0.15   | 0.06                     | 0.017           |      |      |
| IRAS 4A                 |                         | CO      | 2–1  | 117.2                    | 18.4            | 0.07 |      |
|                         | 4–3                     |         | 221.1  | 23.3                     | 0.32            |      |      |
|                         | 6–5                     |         | 121.9  | 13.2                     | 0.59            |      |      |
|                         | 10–9                    |         | 35.7   | 1.9                      | 0.073           |      |      |
|                         | $^{13}\text{CO}$        | 10–9    | 1.2  | 0.2                      | 0.017           |      |      |
|                         | $\text{C}^{18}\text{O}$ | 2–1     | 4.3  | 2.3                      | 0.09            |      |      |
|                         |                         | 5–4     | 0.5  | 0.26                     | 0.005           |      |      |
|                         |                         | 9–8     | 0.1  | 0.05                     | 0.018           |      |      |
|                         |                         | IRAS 4B | CO   | 2–1                      | 54.8            | 13.9 | 0.07 |
|                         |                         |         |  | 4–3                      | 115.2           | 14.6 | 0.26 |
| 6–5                     |                         |         |  | 43.3                     | 7.3             | 0.36 |      |
| 10–9                    | 26.8                    |         |  | 2.6                      | 0.076           |      |      |
| $^{13}\text{CO}$        | 10–9                    |         | 0.7  | 0.15                     | 0.017           |      |      |
| $\text{C}^{18}\text{O}$ | 2–1                     |         | 4.9  | 2.5                      | 0.19            |      |      |
|                         | 5–4                     |         | 0.23   | 0.12                     | 0.005           |      |      |
|                         | 9–8                     | <0.07   | -  | 0.019                    |                 |      |      |

Notes.  $^a$ In 0.5 km s $^{-1}$  bins.

Complementary ground-based spectral line observations of  $^{12}\text{CO}$  6–5 were obtained at the 12-m Atacama Pathfinder EXperiment Telescope (APEX), using the CHAMP $^+$  2 $\times$ 7 pixel array receiver (Güsten et al. 2008). The lower- $J$  spectral lines were obtained from the James Clerk Maxwell Telescope (JCMT) archive and from Jørgensen et al. (2002). Details will be presented elsewhere (Yıldız et al. 2012).

The observed line profiles are presented in Fig. 2.1 and the corresponding line intensities in Table 2.2. For the  $^{12}\text{CO}$  10–9 toward IRAS 2A, the emission from the blue line wing was chopped out due to emission at the reference position located in the blue part of the SVS 13 outflow. A Gaussian fitted to the red component of the line was used to obtain the integrated intensity.

Kristensen et al. (2010) identify three components in the H $_2$ O line profiles centered close to the source velocities: a broad underlying emission profile (Gaussian with FWHM $\sim$ 25–30 km s $^{-1}$ ), a medium-broad emission profile (FWHM $\sim$ 5–10 km s $^{-1}$ ), and narrow self-



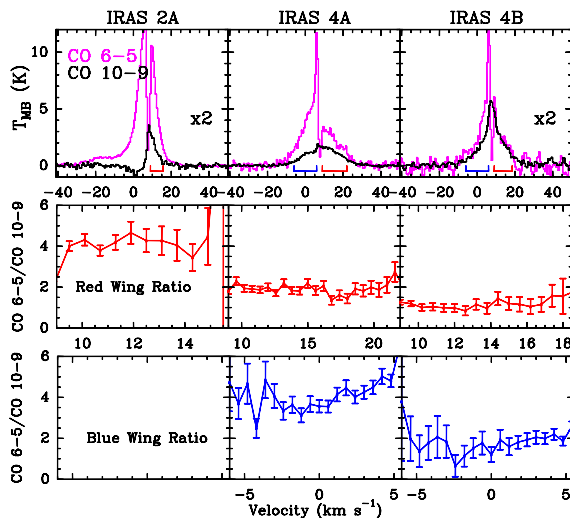


**Figure 2.2** – Ratios of CO 6–5/CO 10–9. *Top*: CO line profiles. The CO 6–5 and 10–9 profiles have been multiplied by a factor of 2 for IRAS 2A and 4B. *Middle and bottom*: ratio of line wing intensity in the specified velocity range indicated in the top panel for the red and blue wings.

absorption lines (FWHM $\sim$ 2–3 km s $^{-1}$ ); see the H $_2$ O 2 $_{02}$ –1 $_{11}$  lines in Fig. 2.1. The same components are also seen in the CO line profiles, albeit less prominently than for H $_2$ O. The broad component dominates the  $^{12}$ CO 10–9 lines of IRAS 4A and 4B and is also apparent in the deep  $^{12}$ CO 6–5 spectrum of IRAS 2A (Fig. 2.2). The medium component is best seen in the  $^{13}$ CO 10–9 profiles of IRAS 4A and 4B and as the red wing of the  $^{12}$ CO 10–9 profile for IRAS 2A. A blow-up of the very high  $S/N$  spectrum of C $^{18}$ O 5–4 for IRAS 4A (insert in Fig. 2.1) also reveals a weak C $^{18}$ O medium-broad profile. The narrow component is clearly observed in C $^{18}$ O emission and  $^{12}$ CO low- $J$  self-absorption. Kristensen et al. (2010) interpret the broad component as shocked gas along the outflow cavity walls, the medium component as smaller-scale shocks created by the outflow in the inner (<1000 AU) dense envelope, and the narrow component as the quiescent envelope, respectively.

## 2.3 Analysis and discussion

### 2.3.1 Broad and medium components: shocked gas

To quantify the physical properties of the broad outflow component, line ratios are determined for the wings of the line profiles. Figure 2.2 shows the CO 6–5/CO 10–9 ratio as a function of velocity. The APEX-CHAMP $^+$  CO 6–5 maps of IRAS 4A and 4B

**Table 2.3** – Summary of column densities,  $N(\text{H}_2)$  in  $\text{cm}^{-2}$  in the broad and medium components in  $20''$  beam.

| Source  | Broad Comp.            | Medium Comp.           |
|---------|------------------------|------------------------|
| IRAS 2A | $6 \times 10^{19}{}^a$ | $2 \times 10^{20}{}^b$ |
| IRAS 4A | $4 \times 10^{20}{}^b$ | $6 \times 10^{20}{}^c$ |
| IRAS 4B | $1 \times 10^{20}{}^b$ | $2 \times 10^{20}{}^c$ |

**Notes.** Obtained from  ${}^a\text{CO 6-5}$ ,  ${}^b\text{CO 10-9}$ ,  ${}^c{}^{13}\text{CO 10-9}$  spectra.

from Yıldız et al. (2012) and IRAS 2A from van Kempen et al. (2009a) are resampled to a  $20''$  beam so that both lines refer to the same beam. The ratios are compared with model non-LTE excitation line intensities calculated using the RADEX code (van der Tak et al. 2007, Fig. 2.4 in the Additional Materials 2.5.1). The density within a  $20''$  diameter is taken to be  $\geq 10^5 \text{ cm}^{-3}$  based on the modeling results of Jørgensen et al. (2002, see also Sect. 2.3.2 and Additional Materials 2.5.2). The detection of medium-broad CS 10–9 emission by Jørgensen et al. (2005b) toward IRAS 4A and 4B indicates densities of the order of a few  $10^6 \text{ cm}^{-3}$ . For the range of densities indicated in Fig. 2.4, the line ratios imply high temperatures: IRAS 2A,  $T_{\text{kin}} = 70\text{--}130 \text{ K}$ ; IRAS 4A,  $T_{\text{kin}} = 90\text{--}120 \text{ K}$ ; and IRAS 4B,  $T_{\text{kin}} = 140\text{--}180 \text{ K}$ .

The optical depth of the  ${}^{12}\text{CO}$  emission is constrained by the  ${}^{12}\text{CO 10-9}/{}^{13}\text{CO 10-9}$  ratios. For IRAS 4B, the optical depth of the  ${}^{12}\text{CO}$  line wings is found to drop with velocity, ranging from  $\tau_{\text{wing}} \sim 12$  near the center to  $\sim 0.4$  at the highest velocities where  ${}^{13}\text{CO}$  is detected. This justifies the assumption that the broad  ${}^{12}\text{CO 10-9}$  lines are optically thin. Total CO column densities in the broad component for these conditions are  $4$  and  $1 \times 10^{16} \text{ cm}^{-2}$  for IRAS 4A and 4B, respectively. For IRAS 2A, the broad column density is calculated from the CO 6–5 spectrum as  $6 \times 10^{15} \text{ cm}^{-2}$ . Using  $\text{CO}/\text{H}_2 = 10^{-4}$  gives the  $\text{H}_2$  column densities listed in Table 2.3.

The medium component attributed to small-scale shocks in the inner envelope can be probed directly by the  ${}^{13}\text{CO 10-9}$  data for IRAS 4A and 4B. For IRAS 2A, the Gaussian fit to the red wing of the  ${}^{12}\text{CO 10-9}$  is used. By assuming a similar range of temperatures and densities as for the broad component, beam averaged  ${}^{12}\text{CO}$  column densities of  $2$ ,  $6$ , and  $2 \times 10^{16} \text{ cm}^{-2}$  are found for IRAS 2A, 4A, and 4B respectively, if the lines are optically thin and using  ${}^{12}\text{C}/{}^{13}\text{C} = 65$ . The very weak medium component found in the  $\text{C}^{18}\text{O 5-4}$  profile for IRAS 4A agrees with this value if the emission arises from a compact (few  $''$ ) source. Assuming  $\text{CO}/\text{H}_2 = 10^{-4}$  leads to the numbers in Table 2.3. The overall uncertainty in all column densities is a factor of 2 due to the range of physical conditions used to derive them and uncertainties in the adopted  $\text{CO}/\text{H}_2$  ratio and calibration. The total amount of shocked gas is  $<1\%$  of the total gas column density in the beam for each source (Jørgensen et al. 2002).

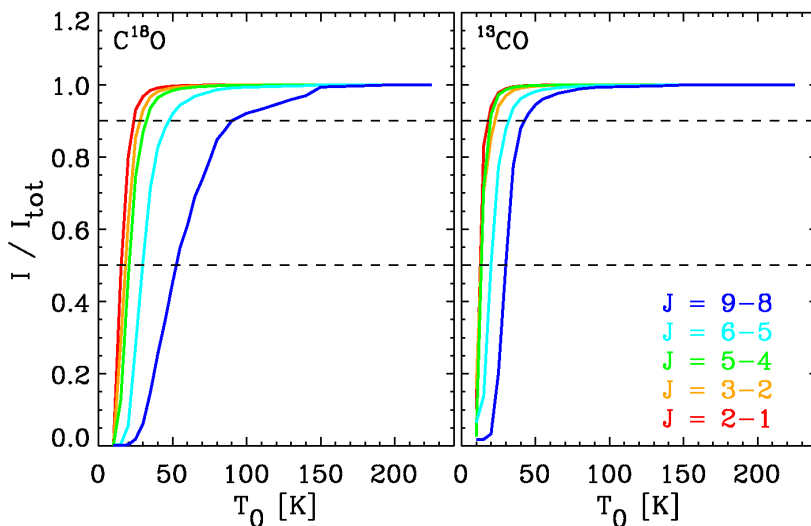


**Figure 2.3** – Dependence of line intensities on temperature  $T_0$  of  $\text{C}^{18}\text{O}$  (left) and  $^{13}\text{CO}$  (right) for an “anti-jump” model of the CO abundance in the IRAS 2A envelope. The line intensities are measured relative to a model where the CO abundance is undepleted at all radii. Each curve therefore represents the fraction of the line intensity for the given transition, which has its origin in gas at temperatures below  $T_0$ . The dashed lines indicate the levels corresponding to 50 and 90% respectively.

### 2.3.2 Narrow component: bulk warm envelope

The narrow width of the  $\text{C}^{18}\text{O}$  emission clearly indicates an origin in the quiescent envelope. Naïvely, one would associate emission coming from a level with  $E_u/k_B=237$  K (9–8) with the warm gas in the innermost part of the envelope. To test this hypothesis, a series of envelope models was run with varying CO abundance profiles. The models were constructed assuming a power-law density structure and then calculating the temperature structure by fitting both the far-infrared spectral energy distribution and the submillimeter spatial extent (Jørgensen et al. 2002). Figure 2.3 compares the fractional line intensities for the  $\text{C}^{18}\text{O}$  and  $^{13}\text{CO}$  transitions in a spherical envelope model for IRAS 2A as a function of temperature. In these models, the abundance in the outer envelope was kept high,  $X_0=2.7\times 10^{-4}$  with respect to  $\text{H}_2$  (all available gas-phase carbon in CO), decreasing by a factor of 1000 at temperatures higher than a specific temperature,  $T_0$  (a so-called ‘anti-jump’ model (see Schöier et al. 2004, for nomenclature)). These models thereby give an estimate of the fraction of the line emission for a given transition (in the respective telescope beams) which has its origin at temperatures lower than  $T_0$ .

For  $\text{C}^{18}\text{O}$ , 90% of the emission in the transitions up to and including the 5–4 HIFI transition has its origin at temperatures lower than 25–30 K, meaning that these transitions are predominantly sensitive to the outer parts of the protostellar envelope. The 9–8 transition

is more sensitive to the warm parts of the envelope, but still 50% of the line flux appears to come from the outer envelope with temperatures less than 50 K. The  $^{13}\text{CO}$  transitions become rapidly optically thick in the outer envelopes: even for the 9–8 transition, 90% of the line flux can be associated with the envelope material with temperatures lower than 40 K.

The  $\text{C}^{18}\text{O}$  9–8 line is clearly a much more sensitive probe of a CO ice evaporation zone than any other observed CO line. Jørgensen et al. (2005c) showed that the low- $J$   $\text{C}^{18}\text{O}$  lines require a drop in the abundance at densities higher than  $7\times 10^4\text{ cm}^{-3}$  due to freeze-out. However, they did not have strong proof for CO evaporation in the inner part from that dataset. Using the temperature and density structure for IRAS 2A as described above, we computed the  $\text{C}^{18}\text{O}$  line intensities in the respective telescope beams following the method by Jørgensen et al. (2005c). In this ‘anti-jump’ model, the outer  $\text{C}^{18}\text{O}$  abundance is kept fixed at  $X_0=5.0\times 10^{-7}$ , whereas the inner abundance  $X_D$  and the freeze-out density  $n_{\text{de}}$  are free parameters. A  $\chi^2$  fit to only the  $\text{C}^{18}\text{O}$  1–0, 2–1 and 3–2 lines gives best-fit values of  $X_D=3\times 10^{-8}$  and  $n_{\text{de}}=7\times 10^4\text{ cm}^{-3}$ , consistent with those of Jørgensen et al. (2005c). However, this model underproduces the higher- $J$  lines by a factor of 3–4 (Fig. 2.6 in Additional Materials).

To solve this underproduction, the inner abundance has to be increased in a so-called ‘drop-abundance’ profile. The fit parameters are now the inner abundance  $X_{\text{in}}$  and the evaporation temperature  $T_{\text{ev}}$ , keeping  $X_D$  and  $n_{\text{de}}$  fixed at the above values. Figure 2.9 in Additional Materials shows the  $\chi^2$  plots to the  $\text{C}^{18}\text{O}$  6–5 and 9–8 lines. The evaporation temperature is not well constrained, but low temperatures of  $T_{\text{ev}}\approx 25\text{ K}$  are favored because they produce more  $\text{C}^{18}\text{O}$  5–4 emission. The best-fit  $X_{\text{in}}=1.5\times 10^{-7}$  indicates a jump of a factor of 5 compared with  $X_D$ . Alternatively,  $T_{\text{ev}}$  can be kept fixed at 25 K and both  $X_{\text{in}}$  and  $X_D$  can be varied by fitting all five lines simultaneously. In this case, the same best-fit value for  $X_{\text{in}}$  is found but only an upper limit on  $X_D$  of  $\sim 4\times 10^{-8}$ . Thus, for this physical model,  $X_{\text{in}} > X_D$ , implying that a jump in the abundance is needed for IRAS 2A.

## 2.4 Conclusions

Spectrally resolved *Herschel*-HIFI observations of high- $J$  CO lines up to  $^{12}\text{CO}$  10–9 and  $\text{C}^{18}\text{O}$  9–8 have been performed toward three low-mass young stellar objects for the first time. These data provide strong constraints on the density and temperature in the various physical components, such as the quiescent envelope, extended outflowing gas, and small-scale shocks in the inner envelope. The derived column densities and temperatures are important for comparison with water and other molecules such as  $\text{O}_2$ , for which HIFI observations are planned. Furthermore, it is shown conclusively that in order to reproduce higher- $J$   $\text{C}^{18}\text{O}$  lines within the context of the adopted physical model, a jump in the CO abundance due to evaporation is required in the inner envelope, something that was inferred, but not measured, from ground-based observations. Combination with even higher- $J$  CO lines to be obtained with *Herschel*-PACS in the frame of the WISH key

program will allow further quantification of the different physical processes invoked to explain the origin of the high- $J$  emission.

## 2.5 Additional materials

### 2.5.1 Radex model

Figure 2.4 shows the CO 6–5/10–9 line ratios for a slab model with a range of temperatures and densities.

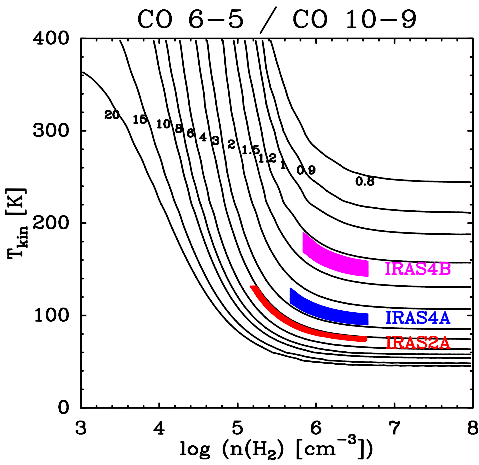


**Figure 2.4** – Model line ratios of CO 6–5/10–9 for a slab model with a range of temperatures and densities. The adopted CO column density is  $10^{17}$  cm<sup>-2</sup> with a line width of 10 km s<sup>-1</sup>, comparable to the inferred values. For these parameters the lines involved are optically thin. The colored lines give the range of densities within the 20'' beam for the three sources based on the models of Jørgensen et al. (2002).

### 2.5.2 Abundance profiles for IRAS 2A

Among the three sources, IRAS 2A has been selected for detailed CO abundance profile modeling because more data are available on this source, and because its physical and chemical structure has been well characterized through the high angular resolution submillimeter single dish and interferometric observations of Jørgensen et al. (2002, 2005a). The physical parameters are taken from the continuum modeling results of Jørgensen et al. (2002). In that paper, the 1D dust radiative transfer code DUSTY (Ivezić & Elitzur 1997) was used assuming a power law to describe the density gradient. The dust temperature as function of radius was calculated self-consistently through radiative transfer given a central source luminosity. Best-fit model parameters were obtained by comparison with the spectral energy distribution and the submillimeter continuum spatial extent. The resulting envelope structure parameters are used as input to the RATRAN radiative transfer modeling code (Hogerheijde & van der Tak 2000) to model the CO line intensities for a

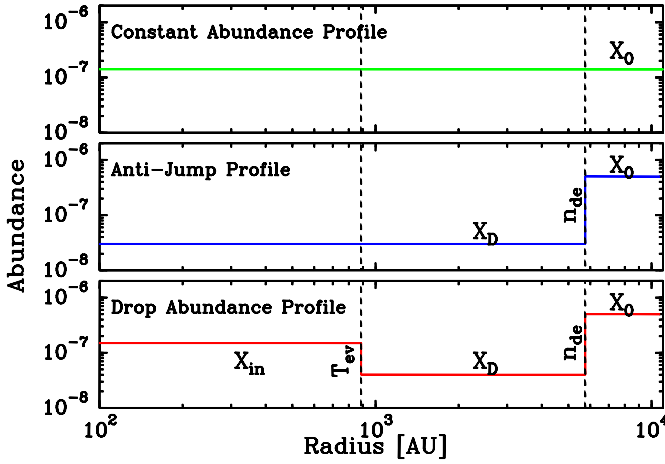


**Figure 2.5** – Examples of constant, anti-jump, and drop abundance profiles for IRAS 2A for  $T_{\text{ev}}=25$  K and  $n_{\text{de}}=7\times 10^4$   $\text{cm}^{-3}$ .

**Table 2.4** – Summary of  $\text{C}^{18}\text{O}$  abundance profiles for IRAS 2A.

| Profile   | $X_{\text{in}}$     | $T_{\text{ev}}$<br>[K] | $X_{\text{D}}$         | $n_{\text{de}}$<br>[ $\text{cm}^{-3}$ ] | $X_0$               |
|-----------|---------------------|------------------------|------------------------|---|---------------------|
| Constant  | -                   | -                      | -                      | -                                       | $1.4\times 10^{-7}$ |
| Anti-jump | -                   | -                      | $3\times 10^{-8}$      | $7\times 10^4$                          | $5\times 10^{-7}$   |
| Drop      | $1.5\times 10^{-7}$ | 25                     | $\sim 4\times 10^{-8}$ | $7\times 10^4$                          | $5\times 10^{-7}$   |

given CO abundance structure through the envelope. The model extends to 11000 AU from the protostar, where the density has dropped to  $2\times 10^4$   $\text{cm}^{-3}$ . The CO- $\text{H}_2$  collisional rate coefficients of Yang et al. (2010) have been adopted.

The  $\text{C}^{18}\text{O}$  lines are used to determine the CO abundance structure because the lines of this isotopologue are largely optically thin and because they have well-defined Gaussian line shapes originating from the quiescent envelope without strong contaminations from outflows. Three types of abundance profiles are examined, namely ‘constant’, ‘anti-jump’ and ‘drop’ abundance profiles. Illustrative models are shown in Fig. 2.5 and the results from these models are summarized in Table 2.4.

### 2.5.2.1 Constant abundance model

The simplest approach is to adopt a *constant abundance* across the entire envelope. However, with this approach, and within the framework of the adopted source model, it is not possible to simultaneously reproduce all line intensities. This was already shown by Jørgensen et al. (2005c). For lower abundances it is possible to reproduce the lower- $J$  lines, while higher abundances are required for higher- $J$  lines. In Fig. 2.6, the  $\text{C}^{18}\text{O}$  spec-

tra of a constant-abundance profile are shown for an abundance of  $X_0=1.4\times 10^{-7}$ , together with the observed spectra of IRAS 2A. Based on these results, the constant-abundance profile is ruled out for all three sources.

### 2.5.2.2 Anti-jump abundance models

The *anti-jump model* is commonly adopted in models of pre-stellar cores without a central heating source (e.g., Bergin & Snell 2002, Tafalla et al. 2004). Following Jørgensen et al. (2005c), an anti-jump abundance profile was employed by varying the desorption density,  $n_{\text{de}}$ , and inner abundance  $X_{\text{in}}=X_{\text{D}}$  in order to find a fit to our observed lines. Here, the outer abundance  $X_0$  was kept high at  $5.0\times 10^{-7}$  corresponding to a  $^{12}\text{CO}$  abundance of  $2.4\times 10^{-4}$  for  $^{16}\text{O}/^{18}\text{O}=550$  as was found appropriate for the case of IRAS 2A by Jørgensen et al. (2005c). This value is consistent with the  $\text{CO}/\text{H}_2$  abundance ratio determined by Lacy et al. (1994) for dense gas without CO freeze-out.

The best fit to the three lowest  $\text{C}^{18}\text{O}$  lines (1–0, 2–1 and 3–2) is consistent with that found by Jørgensen et al. (2005c), corresponding to  $n_{\text{de}}=7\times 10^4 \text{ cm}^{-3}$  and  $X_{\text{D}}=3\times 10^{-8}$  ( $\text{CO}$  abundance of  $1.7\times 10^{-5}$ ). In the  $\chi^2$  fits, the calibration uncertainty of each line (ranging from 20 to 30%) is taken into account. These modeled spectra are overplotted on the observed spectra in Fig. 2.6 as the blue lines, and show that the anti-jump profile fits well the lower- $J$  lines but very much underproduces the higher- $J$  lines.

The value of  $X_0$  was verified a posteriori by keeping  $n_{\text{de}}$  at two different values of  $3.4\times 10^4$  and  $7\times 10^4$ . This is illustrated in Fig. 2.7 where the  $\chi^2$  contours show that for both values of  $n_{\text{de}}$ , the best-fit value of  $X_0$  is  $\sim 5\times 10^{-7}$ , the value also found in Jørgensen et al. (2005c). The  $\chi^2$  contours have been calculated from the lower- $J$  lines only, as these are paramount in constraining the value of  $X_0$ . Different  $\chi^2$  plots were made, where it was clear that higher- $J$  lines only constrain  $X_{\text{D}}$ , as expected. The effect of  $n_{\text{de}}$  is illustrated in Fig. 2.8 for the two values given above.

### 2.5.2.3 Drop-abundance profile

In order to fit the higher- $J$  lines, it is necessary to employ a *drop-abundance* structure in which the inner abundance  $X_{\text{in}}$  increases above the ice evaporation temperature  $T_{\text{ev}}$  (Jørgensen et al. 2005c). The abundances  $X_{\text{D}}$  and  $X_0$  for  $T < T_{\text{ev}}$  are kept the same as in the anti-jump model, but  $X_{\text{in}}$  is not necessarily the same as  $X_0$ . In order to find the best-fit parameters for the higher- $J$  lines, the inner abundance  $X_{\text{in}}$  and the evaporation temperature  $T_{\text{ev}}$  were varied. The  $\chi^2$  plots (Fig. 2.9, left panel) show best-fit values for an inner abundance of  $X_{\text{in}} = 1.5\times 10^{-7}$  and an evaporation temperature of 25 K (consistent with the laboratory values), although the latter value is not strongly constrained. These parameters fit well the higher- $J$   $\text{C}^{18}\text{O}$  6–5 and 9–8 lines (Fig. 2.6). The  $\text{C}^{18}\text{O}$  5–4 line is underproduced in all models, likely because the larger HIFI beam picks up extended emission from additional dense material to the northeast of the source seen in BIMA

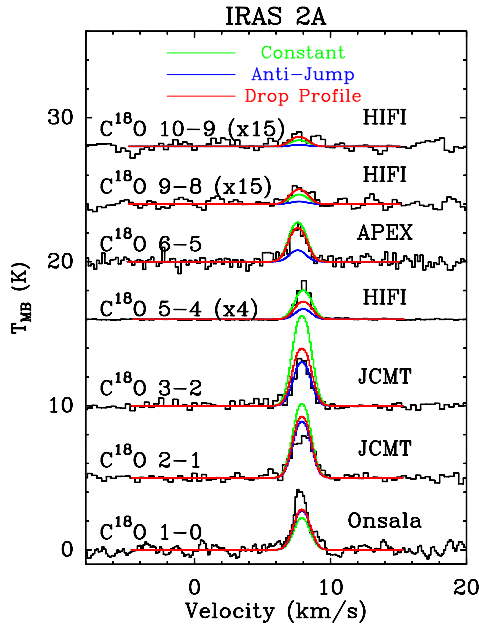


**Figure 2.6** – Best fit constant (green), anti-jump (blue) and drop abundance (red) RATRAN models overlaid on the observed spectra. All spectra refer to single pointing observations. The calibration uncertainty for each spectrum is around 20–30% and is taken into account in the  $\chi^2$  fit. See Table 2.4 for parameters.

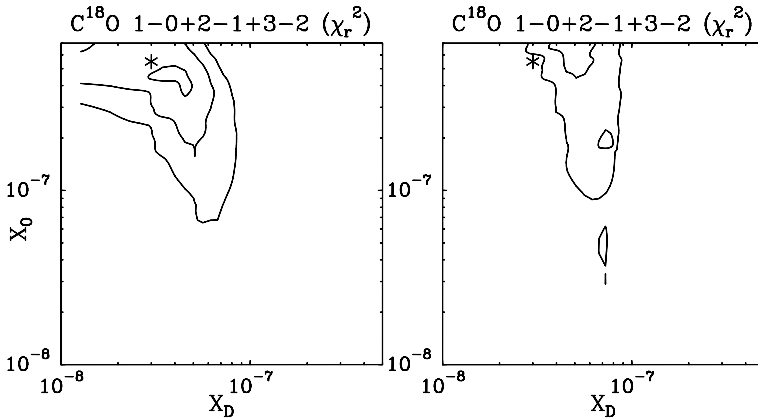


**Figure 2.7** – The  $\chi^2$  plots for the anti-jump profiles where  $X_0$  and  $X_D$  values are varied. *Right*: for  $n_{\text{de}}=7\times 10^4$  and *left*: for  $n_{\text{de}}=3.4\times 10^4\text{ cm}^{-3}$ . The asterisk indicates the value for Jørgensen et al. (2005c) used here. Contours are plotted at the  $2\sigma$ ,  $3\sigma$ , and  $4\sigma$  confidence levels (*left*) and  $3\sigma$  and  $4\sigma$  confidence levels (*right*).

$\text{C}^{18}\text{O}$  1–0 (Volgenau et al. 2006) map.

Because the results do not depend strongly on  $T_{\text{ev}}$ , an alternative approach is to keep



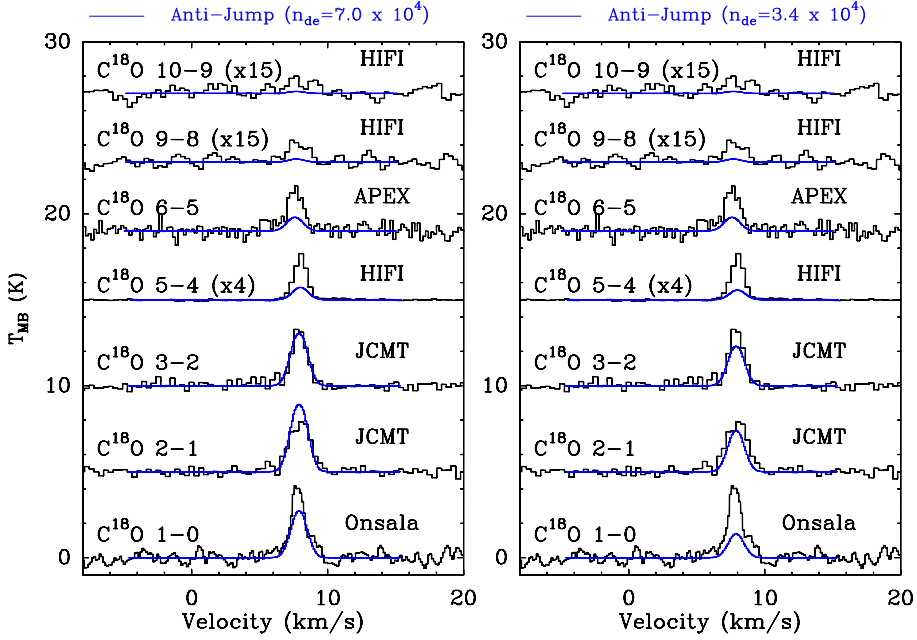


**Figure 2.8** – The IRAS 2A spectra for the  $X_0$  and  $X_D$  parameters corresponding to the values in Jørgensen et al. (2005c) for different  $n_{de}$  values of  $3.4 \times 10^4$  and  $7 \times 10^4$ .

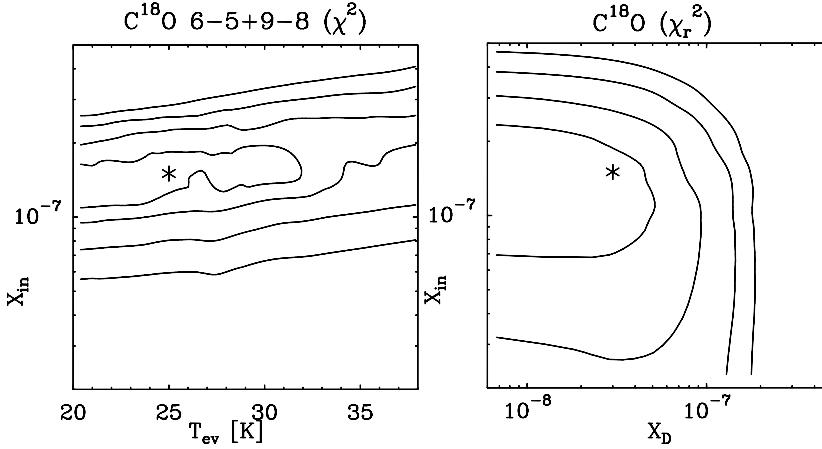


**Figure 2.9** – Reduced  $\chi^2$  plots and best-fit parameters (indicated with \*) for the anti-jump model fit to the lines of  $C^{18}O$  1–0, 2–1, 3–2, 6–5 and 9–8 (right) and for the drop abundance model fit to the higher- $J$  lines of  $C^{18}O$  6–5 and 9–8 (left). Contours are plotted at the  $1\sigma$ ,  $2\sigma$ ,  $3\sigma$ , and  $4\sigma$  confidence levels.

the evaporation temperature fixed at 25 K and vary both  $X_{in}$  and  $X_D$  by fitting both low- and high- $J$  lines simultaneously. In this case, only an upper limit on  $X_D$  of  $\sim 4 \times 10^{-8}$  is

found (Fig. 2.9, right panel), whereas the inferred value of  $X_{\text{in}}$  is the same. This figure conclusively illustrates that  $X_{\text{in}} > X_{\text{D}}$ , i.e., that a jump in the abundance due to evaporation is needed.

The above conclusion is robust within the context of the adopted physical model. Alternatively, one could investigate different physical models such as those used by Chiang et al. (2008), which have a density enhancement in the inner envelope due to a magnetic shock wall. This density increase could partly mitigate the need for the abundance enhancement although it is unlikely that the density jump is large enough to fully compensate. Such models are outside the scope of this paper. An observational test of our model would be to image the  $\text{N}_2\text{H}^+$  1–0 line at high angular resolution: its emission should drop in the inner  $\sim 900$  AU ( $\sim 4''$ ) where  $\text{N}_2\text{H}^+$  would be destroyed by the enhanced gas-phase CO.

## Acknowledgements

*The authors are grateful to many funding agencies and the HIFI-ICC staff who has been contributing for the construction of Herschel and HIFI for many years. HIFI has been designed and built by a consortium of institutes and university departments from across Europe, Canada and the United States under the leadership of SRON Netherlands Institute for Space Research, Groningen, The Netherlands and with major contributions from Germany, France and the US. Consortium members are: Canada: CSA, U.Waterloo; France: CESR, LAB, LERMA, IRAM; Germany: KOSMA, MPIfR, MPS; Ireland, NUI Maynooth; Italy: ASI, IFSI-INAF, Osservatorio Astrofisico di Arcetri-INAF; Netherlands: SRON, TUD; Poland: CAMK, CBK; Spain: Observatorio Astronómico Nacional (IGN), Centro de Astrobiología (CSIC-INTA). Sweden: Chalmers University of Technology - MC2, RSS & GARD; Onsala Space Observatory; Swedish National Space Board, Stockholm University - Stockholm Observatory; Switzerland: ETH Zurich, FHNW; USA: Caltech, JPL, NHSC.*



